The Quasar-mode and Radio-mode Feedback of IRAS 09104+4109

K. Cavagnolo[1*], M. Donahue[2], B. McNamara[1,3,4], G. M. Voit[2], and M. Sun[3]

[1]*Department of Physics and Astronomy, University of Waterloo, Waterloo, ON N2L 3G1, Canada.*
[2]*Department of Physics and Astronomy, Michigan State University, East Lansing, MI, 48824-2320, USA.*
[3]*Perimeter Institute for Theoretical Physics, 31 Caroline St. N., Waterloo, Ontario, N2L 2Y5, Canada*
[4]*Harvard-Smithsonian Center for Astrophysics, 60 Garden Street, Cambridge, MA 02138, USA*
[5]*Department of Astronomy, University of Virginia, Charlottesville, VA, 22904, USA.*

ABSTRACT

We report on new *Chandra* X-ray Observations of IRAS 09104+4109.

Key words: cooling flows – galaxies: clusters: general – galaxies: clusters: individual (IRAS 09104+4109)

1 INTRODUCTION

IRAS 09104+4109 (hereafter, IRAS09) is an uncommon low-redshift ($z = 0.4418$) ultraluminous infrared galaxy (ULIRG; $L_{IR} > 10^{12}$ $L_\odot$). Unlike most ULIRGs, IRAS09 is the brightest cluster galaxy (BCG) in a rich galaxy cluster, but unlike most BCGs, IRAS09 is a Seyfert-2 with 99% of the bolometric luminosity emerging longward of 1 μm due to a heavily-obscured ($N_{H,obs} > 10^{24}$ cm^{-2}) quasar (Kleinmann et al. 1988; Hines & Wills 1993; Fabian et al. 1994; Evans et al. 1998; Franceschini et al. 2000; Iwasawa et al. 2001). The present analysis shows the host cluster, RX J0913.7+4056, has a mass $\sim 10^{15}$ M$_\odot$, a central cooling time $t_{cool} < 1$ Gyr, and a spectroscopically determined (non-grating) mass deposition rate $\dot{M} > 100$ M$_\odot$ yr^{-1}. Even at 0.1 $\dot{M}$, a gas reservoir of more than 10^{10} M$_\odot$ should condense out of the intracluster medium (ICM) onto the BCG in ~ 1 Gyr. However, while $\sim 10^9$ M$_\odot$ of hot dust (Taniguchi et al. 1997) and multiple bright optical nebulae are detected in IRAS09, unlike other Seyfert-2 galaxies, IRAS09 has $< 10^{10}$ M$_\odot$ of CO determined H$_2$ gas (Evans et al. 1998), $< 10^8$ M$_\odot$ of cold dust (Deane & Trentham 2001), and no detected polycyclic aromatic hydrocarbon emission or silicate absorption features (Peeters et al. 2004; Sargsyan et al. 2008). Further, near-IR spectroscopy reveals that IRAS09 emits $\sim 10^{42-43}$ erg s^{-1} in Hα (Crawford & Vanderriest 1996; Evans et al. 1998). If the CO upper limits are correct, then compared to other BCGs, the IRAS09 emission line properties indicate a molecular gas poor galaxy (Edge 2001), accentuating the lack of strong indicators of cold, dusty, molecular gas around such a powerful quasar (QSO).

The IRAS09 gas-to-dust ratio (< 300) is suspiciously small compared to other cooling flow BCGs (typically > 500). The answer to this riddle may be that the QSO in IRAS09 is driving a powerful outflow. Integral field spectroscopy presented by Crawford & Vanderriest (1996) indicates the presence of a > 1000 km s^{-1} emission line outflow coincident with the nucleus.

* Email: kcavagno@uwaterloo.ca

CO observations presented in Evans et al. (1998) were not sensitive to high-velocities, > 300 km s^{-1}, the regime where expelled molecular gas may reside. We demonstrate in this paper that the powerful BCG radio source is driving a supersonic plasma outflow with mechanical power $\sim 10^{44}$ erg s^{-1}. We also show, via detection of an X-ray excess 13-26 kpc NE of the nucleus, radiation from the $\sim 10^{47}$ erg s^{-1} QSO is escaping the nucleus and interacting with the ICM in the same region as strongly photoionized & polarized optical emission are detected.

Based on the radiative, mechanical, and extensible gas-poorness properties of IRAS09, we suggest the system is undergoing a rare phase of BCG assembly where radiative and mechanical feedback, in an approximately 100:1 ratio, are simultaneously conspiring to quench cooling within and around the host galaxy. Numerical simulations suggest such a phase of galaxy assembly should exist, though no conclusive examples have been found. Cosmological simulations typically put radiation- and kinetic-dominated feedback into a distinct early-time quasar-mode (*e.g.* Springel et al. 2005) and a late-time radio-mode (*e.g.* Croton et al. 2006; Bower et al. 2008), respectively. The quasar-mode of feedback is expected to be brief, expelling large quantities of molecular gas from the host galaxy (Narayanan et al. 2006), while the prolonged, intermittent radio-mode heats the host environment, regulating cooling for the rest of the galaxy's life (see McNamara & Nulsen 2007, for a review). Examples of mechanical feedback are many (*e.g.* Fabian et al. 2000b; McNamara et al. 2005), and the best evidence of AGN feedback expelling molecular gas comes from low-luminosity, low-redshift early-type galaxies (*e.g.* Schawinski et al. 2009), but, to our knowledge, IRAS09 is the only system where both are observed **XXX: Is this true?**.

In this paper, we present the argument that IRAS09 is undergoing a crossover between quasar-mode and radio-mode feedback. We explore the possibility that the QSO in IRAS09 has expelled, and/or sufficiently heated, the galactic gas reservoir which provides fuel for the supermassive black hole (SMBH), and that the associated jets are suppressing cooling of the X-ray halo from which the galactic reservoir would be re-supplied. Further, we confirm the

conclusion of Crawford & Vanderriest (1996) that the BCG nebular velocities and gas masses are inconsistent with a scenario where the gas reservoir was deposited by stripping or tidal interactions. Based on the AGN outburst energetics, it is shown that Bondi accretion is unlikely to be responsible for fueling the AGN. We thus conclude that the BCG reached its current state predominately through the influence of cold-mode accretion and a cooling flow. However, this conclusion is limited by the need for deeper sub-mm observations to probe molecular gas mass scales of $\sim 10^9$ $M_\odot$ and velocities > 300 km s^{-1}.

Reduction of X-ray and radio data is discussed in Section 2. ICM global (Section 3) and radial (Section 4) properties are then analyzed. Details regarding the ICM cavities, SMBH fueling, and QSO heating of the ICM are given in Sections 5, 6, and 7, respectively. The complex nuclear source is discussed in Section 8. We provide interpretation of the results throughout and a supply a brief summary in Section 9.

A ΛCDM cosmology with $H_0 = 70$ km s^{-1} Mpc^{-1}, $\Omega_M = 0.27$, and $\Omega_\Lambda = 0.73$ is adopted. For our assumed cosmography, the cluster redshift of $z = 0.4418$ corresponds to ≈ 9.1 Gyr for the age of the Universe, $D_A \approx 5.72$ kpc arcsec^{-1}, and $D_L \approx 2.45$ Gpc. All errors are 90% confidence unless stated otherwise. For all spectral fits, the Galactic absorbing column density was fixed at $N_{H,Gal} = 1.58 \times 10^{20}$ cm^{-2} (Kalberla et al. 2005). Unless otherwise noted, spectral fitting was performed with the χ^2 statistic in XSPEC 12.4.0 (Arnaud 1996) using an absorbed single-temperature MEKAL model (Mewe et al. 1985, 1986) with abundance as a free parameter (Anders & Grevesse 1989 solar abundance distribution assumed) over the energy range 0.7-7.0 keV. For all calculations involving ICM gas, we assume a mean molecular weight of $\mu = 0.597$ and adiabatic index $\gamma = 5/3$.

2   OBSERVATIONS AND DATA REDUCTION

2.1   *Chandra*

A 77.2 ks observation of IRAS09 was taken on 2009 January 09 with the ACIS-I instrument (ObsID 10445; PI Cavagnolo). The 9 ks archival *Chandra* observation of IRAS09 from 1999 November 03 taken with the ACIS-S array was included in our analysis (ObsID 509; PI Fabian). Both datasets were reprocessed and reduced using CIAO and CALDB versions 4.2. X-ray events were selected using *ASCA* grades, and corrections for the ACIS gain change, charge transfer inefficiency, and degraded quantum efficiency were applied. Point sources were located and excluded using WAVDETECT and visual inspection. Light curves from a source free region of each observation were created for a front-illuminated and back-illuminated CCD and compared to look for flares. Time intervals which fell outside 20% of the mean background count rate were excluded. After flare exclusion, the final exposure times for ObsID 509 and 10445 were 7 ks and 76 ks, respectively.

For imaging analysis, the flare-clean events files were reprojected to a common tangent point and summed. The astrometry of the ObsID 509 dataset was improved using a new aspect solution created with the CIAO tool REPROJECT_ASPECT and the positions of several field sources. The positional uncertainty introduced by the strong angle dependence of the off-axis *Chandra* point-spread function (PSF) was minimized by using sources closest to the aim-point. After correction of the astrometry, the positional accuracy between both observations was comparable to the resolution limit of the ACIS detectors. We refer to the final point source free, flare-clean, exposure-corrected images as the "clean" images. In Figure 1 are the 0.5-10.0 keV mosaiced clean image of RX J0913.7+4056, a zoom-in of the core region harboring IRAS09, and photons in the energy range 4.35-4.50 keV associated with the Fe Kα fluorescence line from the nucleus (discussed in Section 8). Unless stated otherwise, the X-ray analysis in this paper relates to the *Chandra* data only.

2.2   *XMM-Newton*

XMM-Newton observed IRAS09 on 2003 April 23 for 14 ks with the EPIC PN and MOS detectors (ObsID 0147671001; PI Fiore). Data was reprocessed using SAS version 7.1 and CCF release 258. Events files were created using the tools EMCHAIN and EPCHAIN for patterns 0-4. Light curves were extracted from the energy range 10-12 keV for the full field after *Chandra* identified point sources and cluster emission were removed. After flare exclusion, the effective exposure times for PN and MOS were 10 ks and 12 ks, respectively. A source spectrum grouped to 20 counts per energy channel was extracted from a region centered on the X-ray peak and extending to R_{500} (defined in Section 3). A background spectrum was extracted from a source-free region with an area equal to the source region. Instrument responses were generated with the tools ARFGEN and RMFGEN. The *XMM-Newton* data is utilized in Section 8 to check our results for the nuclear source against the analysis presented in Piconcelli et al. (2007).

2.3   *BeppoSAX*

Conclusions reached in previous studies regarding the nature of the IRAS09 nuclear absorber have relied on the *BeppoSAX* hard X-ray detection discussed by Franceschini et al. (2000). We retrieved and re-analyzed the *BeppoSAX* PDS X-ray data (15-220 keV) taken 1998 April 18 (ObsCode 50273002; PI Franceschini). The data was reduced and analyzed with SAXDAS version 2.3.1 using the calibration data and cookbook available from HEASARC[1]. PDS data was accumulated, screened for good time intervals, and then a light curve was extracted to look for spikes caused by fluorescence of only one of the four PDS crystal scintillators. No spikes were detected.

A PDS total spectrum was extracted from the on-axis data, and background subtraction was performed using the variable rise time threshold. The epoch appropriate response function used in fitting was selected from the HEASARC database. Following the HEASARC cookbook, LECS and MECS spectra were also generated for the R_{500} region with a background spectrum taken from an annulus outside R_{500}. We measured a PDS 15-80 keV count rate of 0.106 ± 0.055 ct s^{-1}. Fitting the PDS spectrum over the energy range 20-200 keV with an absorbed power-law having fixed spectral index of $\Gamma = 1.7$ yields fluxes of $f_{10-200} = 2.09^{+1.95}_{-1.95} \times 10^{-11}$ erg s^{-1} cm^{-2} and $f_{20-100} = 1.10^{+1.57}_{-1.63} \times 10^{-11}$ erg s^{-1} cm^{-2}. These values are consistent with the results presented in Franceschini et al. (2000). The LECS, MECS, and PDS spectra are utilized in Section 8 to check our results against Franceschini et al. (2000).

2.4   *INTEGRAL & Swift*

Between the beginning of 2005 and end of 2006, IRAS09 was within the *INTEGRAL* field of view (FOV) during 85 pointings. For

---

[1] http://heasarc.nasa.gov/docs/sax/shp_software.html

81 pointings, data was collected with the IBIS Soft Gamma-Ray Imager (ISGRI; E_{sens} = 15 keV-1 MeV), and for 79 pointings data was collected with detector-1 of the Joint European X-ray Monitor (JEM-X; E_{sens} = 3-35 keV). Datasets were reduced using OSA version 8.0 and version 8.0.1 of the Instrument Characteristics. For each instrument, mosaiced images of intensity, significance, variance, and exposure were generated from the background-subtracted images of each pointing. The combined ISGRI and JEM-X effective exposure times are 200 ks and 210 ks, respectively.

Versions 1 and 30 of the *INTEGRAL* Reference Catalogue were used for source detection. The OSA source detection routines did not locate any 5σ sources in the ISGRI and JEM-X mosaiced images. Additional visual inspection of the mosaiced ISGRI and JEM-X images did not reveal any features which might suggest emission from a source. The ISGRI and JEM-X instrument responses have a strong energy dependence, thus, upper limits calculated using only the variance images (*i.e.* assuming uniform sensitivity) will systematically underestimate the flux limit. To account for this variation, flux upper limits were derived by integrating the ISGRI and JEM-X response matrix functions (RMFs) over a specified energy range and weighting by an assumed spectral shape.

We assumed the IRAS09 $E > 10$ keV spectrum goes as $S_\nu = \nu^{-1.7}$ with no high-energy cut-off. Between 10-35 keV and 20-100 keV, we derive 3σ upper limits of $f_{10-35} = 1.28 \times 10^{-12}$ erg s^{-1} cm^{-2} and $f_{20-100} = 5.70 \times 10^{-11}$ erg s^{-1} cm^{-2}, respectively. The *INTEGRAL* 1σ 20-100 keV flux limit is narrowly higher than the *BeppoSAX* 20-100 keV PDS measured flux. The *INTEGRAL* 20-100 keV upper limit is also consistent with a $z = 0.442$ source which would not be detected in the IBIS Extragalactic AGN Survey (Bassani et al. 2006).

As a check of this result, the *Swift*-BAT archive was searched for sources. No sources within $5°$ of IRAS09 were detected in the 22 month *Swift*-BAT survey (Tueller et al. 2010). The *Swift*-BAT survey has a 14-195 keV 4.8σ detection limit of 2.2×10^{-11} erg s^{-1} cm^{-2}, which is 14% higher than the 14-195 keV IRAS09 flux expected based on the *BeppoSAX* detection. Assuming the *INTEGRAL* and *Swift*-BAT upper limits are representative of a $1°$ region around IRAS09 (*i.e.* the FWHM PDS FOV), the lack of detected hard X-ray sources near IRAS09 suggests that the PDS detection did not originate from a brighter off-axis source, assuming the source is/was not transient or a one-off event.

2.5 VLA

Between the years 1986 and 2000, IRAS09 was observed at multiple frequencies with varying resolutions using the VLA radio observatory. Continuum mode observations were taken from the VLA archive and reduced using version 3.0.0 of the Common Astronomy Software Applications (CASA). Flagging of bad data was performed using a combination of CASA's FLAGDATA tool in RFI mode and manual inspection. Radio images were generated by Fourier transforming, cleaning, self-calibrating, and restoring individual radio observations. The additional steps of phase and amplitude self-calibration were included to increase the dynamic range and sensitivity of the radio maps. All sources within the primary beam and first sidelobe detected with fluxes $> 5\sigma_{rms}$ were imaged to further maximize the sensitivity of the radio maps.

Resolved radio emission associated with IRAS09 is detected at 1.4 GHz, 5 GHz, and 8.4 GHz, while a 3σ upper limit of 0.84 mJy is established at 14.9 GHz. Fluxes for unresolved emission at 74 MHz, 151 MHz, and 325 MHz were retrieved from the VLA Low-Frequency Sky Survey (VLSS; Cohen et al. 2007), 7C Survey

(Riley et al. 1999), and Westerbork Northern Sky Survey (WENSS; Rengelink et al. 1997), respectively. No formal detection is found in VLSS, however, an overdensity of emission at the location of IRAS09 is evident. For completeness, we measured a flux for the potential source, but excluded the value during fitting of the radio spectrum. The combined 1.4 GHz image reveals the most extended structure, and thus our discussion regarding radio morphology is guided using this frequency. An analysis of 1.4 and 5 GHz VLA data is also presented in Hines & Wills (1993, hereafter H93).

The resolution of the combined 1.4 GHz dataset is $0.37''$ pixel^{-1} with an average beam shape of $1.26'' \times 1.15''$ inclined at $-37.16°$ from north and an off-source rms noise of 0.027 mJy beam^{-1}. The deconvolved, integrated 1.4 GHz flux of the continuous extended structure coincident with IRAS09, and having $S_\nu \gtrsim 3\sigma_{rms}$, is 14.0 ± 0.51 mJy. A significant spur of radio emission northeast of the nucleus is detected with flux 0.21 ± 0.07 mJy. Radio contours were generated beginning at 3 times the rms noise and moving up in 6 log-space steps to the peak intensity of 4.7 mJy beam^{-1}. These are the contours referenced in all following discussion of the radio source morphology and its interaction with the X-ray gas.

To investigate properties of the radio source, we fitted the radio spectrum between 151 MHz and 8.4 GHz for the full radio source (lobes, jets, & core) with the well-known KP (Kardashev 1962; Pacholczyk 1970), JP (Jaffe & Perola 1973), and CI (Heavens & Meisenheimer 1987) synchrotron models. The models vary by assumption of pitch-angle distribution and number of electron injections. The models were fitted to the radio spectrum using the code of Waters & Zepf (2005), which is based on the method of Carilli et al. (1991). The JP model (single electron injection, randomized but isotropic pitch-angle distribution) yields the best fit with $\chi^2(DOF) = 0.491(3)$, a break frequency of $\nu_B = 12.9 \pm 1.0$ GHz, and a low-frequency ($\nu < 2$ GHz) spectral index of $\alpha = -1.10 \pm 0.09$. The radio spectrum and best-fit models are shown in Figure 2. The bolometric radio luminosity was approximated by integrating under the JP curve between $\nu_1 = 10$ MHz and $\nu_2 = 10,000$ MHz, giving $L_{radio} = 1.09 \times 10^{42}$ erg s^{-1}.

Assuming inverse-Compton (IC) scattering and synchrotron emission are the dominant radiative mechanisms of the radio source, the time since the radiating particles were last accelerated is given by Slee et al. (2001) as

$$t_{sync} = 1060 \left(\frac{B^{1/2}}{B^2 + 0.67 B_m^2} \right) \left[\nu_B (1+z) \right]^{-1/2} \text{ Myr} \quad (1)$$

where B [μG] is magnetic field strength, $B_m = 3.25(1+z)^2$ [μG] is a correction for IC losses to the cosmic microwave background, ν_B [GHz] is the radio spectrum break, and z is the dimensionless source redshift. We assume that B can be approximated by the equipartition magnetic field strength, B_{eq}, derived from the minimum energy density condition (Miley 1980),

$$B_{eq} = \left[\frac{6\pi c_{12}(\alpha, \nu_1, \nu_2) L_{radio} (1+k)}{V\Phi} \right]^{2/7} \mu\text{G} \quad (2)$$

where $c_{12}(\alpha, \nu_1, \nu_2)$ is a dimensionless constant derived in Pacholczyk (1970), L_{radio} [erg s^{-1}] is the integrated radio luminosity from ν_1 to ν_2, k is the dimensionless ratio of lobe energy in non-radiating particles to that in relativistic electrons, V [cm^3] is the radio source volume, and Φ is a dimensionless radiating population volume filling factor. Synchrotron age curves as a function of k and Φ are given in Figure 2. The various combinations of k and Φ give $B_{eq} \approx 4$–56 μG and associated synchrotron ages in the

range $\approx$ 6–22 Myr. Our synchrotron ages do not account for energy lost to adiabatic expansion of the radio plasma and should be considered upper limits (Scheuer & Williams 1968).

3   GLOBAL ICM PROPERTIES

Our analysis begins at the cluster scale with the integrated properties of the RX J0913.7+4056 ICM hosting IRAS09. We define the mean cluster temperature, T_{cl}, as the ICM temperature within a core-excised aperture extending to R_{Δ_c}, the radius at which the average cluster density is Δ_c times the critical density for a spatially flat Universe. We chose $\Delta_c = 500$ and used the relations from Arnaud et al. (2002) to calculate R_{Δ_c}. IRAS09 has a luminous, cool core which is not representative of T_{cl}, thus, the convention of Maughan (2007) was followed and emission inside $0.15\,R_{500}$ was excised. Source spectra were extracted from the region 0.15–1.0 R_{500} and background spectra were extracted from reprocessed CALDB blank-sky backgrounds (see Section 4). Because T_{cl} and R_{Δ_c} are correlated in the adopted definitions, they were recursively determined until three consecutive iterations produced T_{cl} values which agreed within the 68% confidence intervals. We measure $T_{cl} = 7.54^{+1.76}_{-1.15}$ keV corresponding to $R_{500} = 1.16^{+0.27}_{-0.19}$ Mpc. Measurements for a variety of R_{Δ_c} apertures are summarized in Table 1.

The cluster gas and gravitational masses were derived using the deprojected radial electron density and temperature profiles presented in Section 4. Electron gas density, n_e, was converted to total gas density as $n_g = 1.92 n_e \mu m_H$ where m_H [g] is the mass of hydrogen. The gas density profile was fitted with a β-model (Cavaliere & Fusco-Femiano 1978), and the temperature profile was fitted with the 3D-$T(r)$ model of Vikhlinin et al. (2006) to ensure continuity and smoothness of the radial log-space derivatives when solving the hydrostatic equilibrium equation. Total gas mass was calculated by assuming spherical symmetry and integrating the best-fit β-model out to R_{200}, giving $M_{gas}(r < R_{200}) = 7.99\,(\pm 0.65) \times 10^{13}$ M$_\odot$. The gravitating mass was derived by solving the hydrostatic equilibrium equation using the analytic density and temperature profiles. We calculate $M_{grav}(r < R_{200}) = 7.22\,(\pm 1.44) \times 10^{14}$ M$_\odot$. The ratio of gas mass to gravitating mass is 0.11 ± 0.02. The gas and gravitating mass errors were estimated from 10,000 Monte Carlo realizations of the measured density and temperature profiles and their associated uncertainties.

With the exception of the strange ULIRG/QSO BCG at its heart, RX J0913.7+4056 is a typical, relaxed massive cluster. None of the integrated X-ray cluster properties suggest the system has undergone a recent major merger or cluster-scale AGN outburst which may have dramatically disrupted the cluster. The lack of a detected radio halo also suggests no recent merger activity, previous powerful AGN outbursts, and possibly no turbulent motions in the core (Ferrari et al. 2008). In terms of the galaxy cluster population, RX J0913.7+4056 resides toward the high-end of the mass distribution with a luminosity-temperature ratio and gas fraction consistent with flux-limited and representative cluster samples (Reiprich & Böhringer 2002; Pratt et al. 2009). Adjusted for differences in assumed cosmology, within the uncertainties our measurements agree with prior IRAS09 studies (*e.g.* Allen 2000).

4   RADIAL ICM PROPERTIES

We now discuss the finer structure of the ICM pervading RX J0913.7+4056 via radial ICM properties. Consistent with the global analysis, the nuclear source was excluded from all radial analysis (see comments for Table 1). Temperature and abundance profiles were created using circular annuli centered on the cluster X-ray peak and containing 2.5K and 5K source counts per annulus, respectively. A deprojected temperature profile was generated using the DEPROJ method in XSPEC. We use the projected profile in all analysis as it does not significantly differ from the deprojected profile. Spectra were grouped to 25 source counts per energy channel. CALDB blank-sky backgrounds were reprocessed and reprojected to match each observation, and then normalized for variations of the hard-particle background using the ratio of blank-sky and observation 9.5-12 keV count rates. Following the method outlined in Vikhlinin et al. (2005), a fixed background component was included during spectral analysis to account for the spatially-varying Galactic foreground (see Cavagnolo et al. 2008b, for more detail). The temperature and abundance profiles are shown in the top row of Figure 3.

A surface brightness profile was extracted using concentric $1''$ wide circular annuli centered on the cluster X-ray peak. From the surface brightness and temperature profiles, a deprojected electron density profile was derived using the Kriss et al. (1983) technique (see Cavagnolo et al. 2009a, for more detail). Errors for the density profile were estimated from 10,000 Monte Carlo bootstrap resamplings of the original surface brightness profile. The surface brightness and electron gas density profiles are shown in the second row of Figure 3.

Total gas pressure ($p = 2.4 k T_X n_e$), entropy ($K = k T_X n_e^{-2/3}$), cooling time ($t_{cool} = 3 n k T_X \,[2 n_e n_H \Lambda(T,Z)]^{-1}$), and enclosed X-ray luminosity profiles were also created. These profiles are presented in the bottom two rows of Figure 3. Uncertainties for each profile were calculated by propagating the individual parameter errors and then summing in quadrature. The cooling functions, $\Lambda(T,Z)$, used to calculate cooling times were derived from the best-fit spectral model for each annulus of the temperature profile and interpolated onto the grid of the higher resolution density profile. We also fitted the entropy model $K(r) = K_0 + K_{100}(r/100 \text{ kpc})^\alpha$ to the entropy profile and found best-fit values of $K_0 = 12.6 \pm 2.9$ keV cm^2, $K_{100} = 139 \pm 8$ keV cm^2, and $\alpha = 1.71 \pm 0.10$. After masking out all substructure and the central $2''$, a grouped spectrum for the central 20 kpc was fitted with a thermal model plus cooling flow component. The best-fit model had a mass deposition rate of $\dot{M} = 206^{+87}_{-65}$ M$_\odot$ for upper and lower temperatures of 5.43 keV and 0.65 keV, respectively, with abundance 0.51 $Z_\odot$.

The RX J0913.7+4056 ICM structure is typical of the cool core class of galaxy clusters, with a temperature profile that rises with increasing radius and an entropy profile with a relatively small, flattened core. There are no resolved discontinuities in the temperature, density, or pressure profiles to suggest the presence of a shock or cold front. The entropy profile is consistent with the cool core population as a whole (Cavagnolo et al. 2009a), and, in particular, with the population of $K_0 < 30$ keV cm^2 clusters that have radio-loud AGN and star formation in the BCG (Cavagnolo et al. 2008a). The $K_0 \lesssim 30$ keV cm^2 scale also defines an entropy regime in which thermal electron conduction in cluster cores inefficiently suppresses widespread environmental cooling (Voit et al. 2008). Therefore, core sub-systems, such as parcels of gas uplifted by an AGN, ram pressure stripped gas, or filamentary thermal instabilities, should be long-lived.

Using the RX J0913.7+4056 radial density structure, the ram pressure stripping analysis presented in Kirkpatrick et al. (2009) was performed to investigate how much of the BCG gas reservoir could be deposited by the 6 compact spheroids ($r < 2.5$ kpc; $M_V > -17$ mag) within 80 kpc of the BCG (Soifer et al. 1996; Armus et al. 1999). We estimated a cluster velocity dispersion of $\sigma_{gal} \approx 1109 \pm 259$ km s^{-1} using the relations from Xue & Wu (2000). The ICM density dictates that only 10^{11-12} M$_\odot$ spirals will be efficiently stripped if they are traveling at > 700 km s^{-1} inside of 37 kpc. Our analysis indicates even if 6 gas-rich galaxies ($M_{gas} = 2$–5×10^8 M$_\odot$) were stripped bare, they still contribute 5-10 times too little gas to explain the reservoir in IRAS09.

If the spheroids are instead tidally-truncated compact ellipticals similar to M32, it is odd that the mean projected separation among them is 30 ± 15 kpc, 8-15 times the expected tidal radius of each object. If the spheroids have interacted with each other, or the BCG, to the point of tidal truncation, then to have such large separations requires huge relative velocities. Yet, the BCG nebulae which may have been stripped from the spheroids have small velocities relative to the BCG (Crawford & Vanderriest 1996). But the relaxation and dynamical friction time scales in the core are $\sim 10^{8-9}$ yr, 10-100 times the free-fall time, so if the gas is old enough to have slowed, then it should have fallen into the BCG, unless the gas has high angular momentum or is in a stable orbit.

If mergers are responsible for the accumulation of cold gas in the core, it is odd that the radio source is very linear. Bulk motion and turbulence induced by mergers would disrupt the radio plasma (*e.g.* Simionescu et al. 2009, 2010), indicating that the core has been mostly undisturbed for > 22 Myr. Alternatively, mergers could have been very gentle so as not to stir the core gas, but then how was gas stripped from the galaxies? We thus conclude that the gas reservoir likely did not result from mergers, but most likely from a cooling flow.

5 ICM CAVITY SYSTEM

To aid investigation of ICM substructure, a residual X-ray image was created by subtracting a surface brightness model from the mosaiced *Chandra* clean image. The *Chandra* clean image was binned by a factor of 2 and the surface brightness isophotes fitted with ellipses. The geometric parameters ellipticity (ε), position angle (ϕ), and centroid (X_0, Y_0) were initially free to vary, but the best-fit values for each isophote converged to mean values of $\varepsilon = 0.52 \pm 0.02$, $\phi = 72.5° \pm 1.7°$, and $(X_0, Y_0) = 09^h13^m45^s.5, +40°56'28''$ (J2000). These values were then fixed in the fitting routine to eliminate isophotal twisting which results from statistical variation of the best-fit values for each radial step.

A surface brightness model normalized to the parent image was constructed from the best-fit isophote ellipses and subtracted from the parent image. The resulting residual image is shown in Figure 4. The faint surface brightness decrements NE and SW of the nucleus in the parent image are resolved into cylindrical voids in the residual image. The void and radio jet morphologies closely trace each other, confirming they share a common origin in the AGN outburst. Based on a 1994 *ROSAT* HRI observation, Fabian & Crawford (1995) suggested the presence of a "hole" in the core of RX J0913.7+4056 which was attributed to absorption by a $\dot{M} > 1000$ M$_\odot$ yr^{-1} cooling flow. Using the new *Chandra* observation as a guide, we find the hole is wedged between the nuclear source and the SE cavity. The true cavities are not resolved in the 1994 HRI image, and a longer HRI observation from 1995

did not resolve the cavities. Cavities are a well-known feature of groups and clusters (*e.g.* Bîrzan et al. 2004; Dunn et al. 2005), but currently, IRAS09 is the highest redshift object where cavities have been directly imaged. In addition, IRAS09 is thus far the only example of a QSO system with an unambiguous cavity detection.

The AGN outburst energetics were investigated by calculating the time averaged cavity energy, P_{cav} (see McNamara & Nulsen 2007, for a review). Note that P_{cav} does not account for energy which may be in unresolved shocks, and that P_{cav} is assumed to be a good estimate of the physical quantity jet power, P_{jet}. For the following calculations the cavities were treated as symmetric cylinders. Properties of the individual cavities are listed in Table 3.

The $4pV$ work to create the cavities was calculated by integrating the high-resolution pressure profile over the surface of each cylinder. The radio source morphology, spectrum, and age suggest the jets were recently, or still are, being fed by the central source. Thus, we assumed the cavities are being excavated on a timescale dictated by the ambient gas sound speed, t_{sonic} (see Bîrzan et al. 2004), and are not buoyant structures. We set the distance of the cavity as its leading edge when calculating t_{sonic}, not the cavity mid-point, as is common in many other studies. A systematic uncertainty of 10% was included to account for error in cavity geometric parameters and from assuming $\Delta(kT_X) = 0$ over the length of the cavities. We calculate a total cavity power of $P_{cav} = 3.41(\pm 0.82) \times 10^{44}$ erg s^{-1}. Radio luminosity has been shown to also be a reasonable surrogate for measuring total jet power (Bîrzan et al. 2008). Using the Cavagnolo et al. (2009b) P_{jet}-P_{radio} scaling relations, the IRAS09 1.4 GHz & 325 MHz powers correspond to $P_{jet} \sim 2$–6×10^{44} erg s^{-1}, in agreement with the X-ray determined value.

The lower limit for t_{sonic} is 42 Myr, but the radio source is less than 22 Myr old. For the radio plasma to still be synchrotron-loud throughout the jet requires constant injection from the AGN, which is ruled out by the radio spectral properties, or that the AGN outflow is supersonic. Compared to the ICM sound speed, the velocity required to reach the end of the radio jet in 22 Myrs suggests $M = 2.3$. If the outflow is supersonic, then local gas shocking may have occurred. However, the X-ray analysis and nebular properties indicate no shocks are present (Crawford & Vanderriest 1996; Tran et al. 2000), so the estimates presented next are poorly constrained. We estimated the outburst energy including shocks to be $\approx 10^{46}$ erg s^{-1} by setting $t_{sonic} = 22$ Myr and multiplying up by a factor of M^3 since $\Delta P_{cav} = \Delta p / \Delta t$ and $\Delta p \propto M^3$.

Within the formal uncertainties, the AGN ourburst energy is on the order of a few times 10^{44} erg s^{-1} with a maximal value of 10^{46} erg s^{-1}. Compared with other systems hosting cavities, IRAS09 resides between the middle and upper-end of the cavity power distribution. The AGN outburst is powerful, but there is nothing unusual about the energetics given the cluster mass and ICM properties.

Of interest is how the AGN energetics compare to the cooling rate of the host X-ray halo. The cooling radius was set at the radius where the ICM cooling time is equal to H_0^{-1} at the redshift of IRAS09. We calculate $R_{cool} = 128$ kpc, and measure an unabsorbed bolometric luminosity within this radius of $L_{cool} = 1.61^{+0.25}_{-0.20} \times 10^{45}$ erg s^{-1}. If all of the cavity energy is thermalized over 4π sr, then $\approx 20\%$ of the energy radiated away by gas within R_{cool} is offset by the ongoing AGN outburst. This highly optimistic scenario implies that five such AGN outbursts will significantly suppress cooling of the gaseous halo.

6   FUELING THE AGN OUTBURST

An estimate of black hole mass, M_{BH}, is key to investigating what powers an AGN outburst. There are a variety of M_{BH} estimators, many of which rely on near-IR, far-IR, and optical emission line diagnostics (Marconi & Hunt 2003; Graham 2007; McGill et al. 2008). However, the IR and emission line properties of IRAS09 may not be representative of the bulge stellar component, but hot dust and complex nebulae. Therefore, we calculated M_{BH} using a variety of relations and took their weighted mean. Using the corrected B-band magnitude from HyperLeda[2], we calculated a BCG stellar velocity dispersion of $\sigma_s = 293 \pm 6$ km s^{-1} from the Faber & Jackson (1976) relation. Inserting this value into the Tremaine et al. (2002) relation gives $M_{BH} = 0.63 (\pm 0.05)$ M$_9$ where M$_9 = 10^9$ M$_\odot$. Using the Graham (2007) relations which relate the absolute $[B,R,K]$-band magnitudes to M_{BH}, we find $M_{BH} = 0.64$–4.1 M$_9$. The final weighted mean value is $M_{BH} = 1.05 \pm 0.17$ M$_9$.

The gravitational binding energy of the material accreting onto the SMBH is transported outward via relativistic jets. Assuming this conversion has some efficiency, ε, then the energy deposited in cavities by the jets implies an accretion mass expressed as $M_{acc} = H_{cav}/(\varepsilon c^2)$ with a time-averaged mass accretion rate of $\dot{M}_{acc} = M_{acc}/t_{sonic}$. Assuming $\varepsilon = 0.1$, the AGN outburst resulted from the accretion of $3.19\,(\pm 0.35) \times 10^6$ M$_\odot$ at a rate of 0.06 ± 0.01 M$_\odot$ yr^{-1}. The mass-energy going into the SMBH and not the jets is expressed as $\Delta M_{BH} = (1 - \varepsilon) M_{acc}$ with a time-averaged rate of $\dot{M}_{BH} = \Delta M_{BH}/t_{sonic}$. The black hole mass thus grew by $2.87\,(\pm 0.31) \times 10^6$ M$_\odot$ at a rate of 0.05 ± 0.01 M$_\odot$ yr^{-1}.

Assuming spherical symmetry, the accretion flow feeding the SMBH can be characterized in terms of the Eddington (Eqn. 3) and Bondi (Eqn. 4) accretion rates,

$$\dot{M}_{Edd} = \frac{2.2}{\varepsilon} \left(\frac{M_{BH}}{10^9 \, M_\odot} \right) \, M_\odot \, yr^{-1} \qquad (3)$$

$$\dot{M}_{Bon} = 0.013 \, K_{Bon}^{-3/2} \left(\frac{M_{BH}}{10^9 \, M_\odot} \right)^2 \, M_\odot \, yr^{-1} \qquad (4)$$

where K_{Bon} [keV cm^2] is the mean entropy of gas within the Bondi radius. The Eddington rate defines the maximal inflow rate of gas not expelled by radiation pressure, as where the Bondi rate approximates the quantity of hot ambient gas captured by the SMBH, *i.e.* hot-mode accretion. Assuming $\varepsilon = 0.1$ and $K_{Bon} = K_0$, the derived M_{BH} gives $\dot{M}_{Edd} \approx 23$ M$_\odot$ yr^{-1} and $\dot{M}_{Bon} \approx 3.2 \times 10^{-4}$ M$_\odot$ yr^{-1}. Thus, the Eddington and Bondi ratios for the accretion event which powered the AGN outburst are $\dot{M}_{acc}/\dot{M}_{Edd} \approx 0.003$ and $\dot{M}_{acc}/\dot{M}_{Bon} \approx 300$.

The Bondi radius for IRAS09 is unresolved ($R_{Bon} = 9$ pc), and K_{Bon} is likely less than K_0. For a Bondi ratio of at least unity, K_{Bon} must be $\leqslant 0.34$ keV cm^2, lower than is measured for even galactic coronae (Sun et al. 2007). In terms of entropy, $t_{cool} \propto K^{3/2} \, kT_X^{-1}$ (Donahue et al. 2006). Assuming gas close to R_{Bon} is no cooler than 0.5 keV, the accreting material will have $t_{cool} < 6$ Myr, a factor of 60 below the shortest ICM cooling time and 1/4 the free-fall time in the core. But this creates the problem that gas close to R_{Bon} is disconnected from cooling at larger radii, breaking the feedback loop (Soker 2006). If instead cold-mode accretion dominates, then the gas which becomes fuel for the AGN is distributed in the BCG halo, $r \sim 1$–30 kpc, and falls into the BCG as a result of cooling (Pizzolato & Soker 2005, 2010). Indeed, *HST* WFPC2

2 http://leda.univ-lyon1.fr

images reveal radial filaments and gaseous substructure down to the resolution-limit within 30 kpc of IRAS09 (Armus et al. 1999). This may indicate cooling, overdense regions similar to the cold blobs expected in cold-mode accretion. The process of cold-mode accretion is more consistent with the nature of IRAS09, and though Bondi accretion cannot be ruled out, it does not seem viable, and may not be in general for cool core BCGs (McNamara et al. 2010).

Unlike most clusters with cavities where AGN mechanical feedback energetically dominates, IRAS09 is radiatively-dominated by a heavily obscured QSO with a bolometric luminosity of $L_{bol}^{QSO} \approx 1 \times 10^{47}$ erg s^{-1} (see Section 8). Assuming the mass accretion powering the QSO goes as $\dot{M}_{acc} = L_{bol}^{QSO}/(\varepsilon c^2)$ with $\varepsilon = 0.1$, then $\dot{M}_{acc} \approx 19$ M$_\odot$ yr^{-1}. Hence, the Eddington ratio for the accretion powering the QSO is $\dot{M}_{acc}/\dot{M}_{Edd} \approx 0.80$. Fabian et al. (2009, hereafter F09) demonstrated that AGN radiation pressure has a significant influence on the mean density of dusty material in the host galaxy. In the formalism of F09, the IRAS09 AGN has an effective Eddington ratio of $\lambda_{Edd} = L_{bol}^{QSO}(1.38 \times 10^{38} \, M_{BH})^{-1} \approx 0.72$. In the N_H-λ_{Edd} plane presented by F09, IRAS09 resides very near the boundary between the regions where AGN obscuring clouds are long-lived and where dusty clouds experience the effects of a super-Eddington AGN, *i.e.* where clouds are efficiently expelled. We point out that these estimates are at the mercy of our choice for M_{BH}. If M_{BH} is $\geqslant 5$ M$_9$, the Eddington ratios will be < 0.2, as where $M_{BH} < 1$ M$_9$ implies Eddington ratios > 1.

7   ICM SUBSTRUCTURE & QSO IRRADIATION

In Figure 4, three regions of X-ray emission in excess of the best-fit surface brightness model are highlighted. The regions are illustrative and approximate the constant surface brightness contours used to define the spectral extraction regions. Each region is denoted by its location relative to the nucleus: northern excess (NEx), eastern excess (EEx), and western excess (WEx). The NEx and WEx appear to be part of a tenuous, arc-like filament which may be gas displaced by the NW radio jet. Similar features are found around other cavity systems (*e.g.* Blanton et al. 2009), but the data is insufficient to determine if this is the case for IRAS09, hence we treat them as separate structures.

Spectral analysis was performed on each region. A background spectrum was extracted from regions neighboring the excesses which did not show enhanced emission in the residual image. The backgrounds were scaled to correct for differences in sky area. For each region, the ungrouped source and background spectra were differenced in XSPEC to create a residual spectrum. To avoid systematically cooler best-fit temperatures resulting from low count rates (Nousek & Shue 1989), the modified Cash statistic (Cash 1979) was used during fitting. The low signal-to-noise ratio (SN) of each spectrum precluded setting metal abundance as a free parameter when fitting a thermal model. The three excesses reside within the two central annuli of the abundance profile, thus abundance was fixed at 0.51 $Z_\odot$. Varying the fixed abundance by ± 0.2 $Z_\odot$ changed the output temperatures and normalizations within the statistical uncertainties when 0.51 $Z_\odot$ was assumed. A fixed thermal component scaled to sky area representing the ICM emission for the coincident annulus was included in the fitting.

The NEx residual spectrum had low-SN which resulted in poor resolution of spectral features. The NEx thermal model had an unconstrained temperature of ~ 7 keV, similarly the power-law model had an unconstrained spectral index of $\Gamma \sim 1.9$. The northern radio jet terminates in the NEx region, and the hardness ratio

map (see Section 8 and Figure 4) shows a possible hot spot in this same area. The NEx may result from non-thermal emission in the hot spot, but we cannot confirm this spectroscopically.

The EEx and WEx residual spectra have characteristics consistent with thermal emission. The best-fit values for the thermal models are given in Table 2. The EEx spectrum has prominent features at $E < 2$ keV which were poorly fit by a single-component thermal model. The thermal Fe Kα complex was also poorly fit because of an obvious asymmetry toward lower energies. To reconcile the poor fit, three Gaussians were included in the fitting. Comparison of fit statistics and goodness of fits determined from 10,000 Monte Carlo simulations of the best-fit spectra suggest the model with the Gaussians is preferred. The strength of the features relative to the continuum suggest a thermal origin is unlikely, and that the features may be emission line blends.

Hines et al. (1999, hereafter H99) suggested the AGN which produced the large-scale radio jets has been reoriented within the last few Myrs, resulting in a new beaming direction close to the line of sight and at roughly a right angle to the previous beaming axis. The new AGN axis suggested by H99 is coincident with the EEx, the 3σ radio spur northeast of the radio core, a UV ionization cone (H93), an ionized optical nebula (Crawford & Vanderriest 1996; Armus et al. 1999), and highly polarized diffuse optical emission (Tran et al. 2000). A schematic of these respective features is shown in Figure 4. Russell et al. (2010) show that the QSO in H1821+643, which is a factor of 10 more powerful than IRAS09, is capable of photoionizing gas up to 30 kpc from the nucleus, and we suspected a similar process may be occurring in IRAS09.

To test this hypothesis, reflection and diffuse spectra were simulated for the nebula and ICM coincident with the EEx using CLOUDY (Ferland et al. 1998). The nebular gas density and ionization state were taken from Tran et al. (2000), while the initial ICM temperature, density, and abundance were set at 3 keV, 0.04 cm^{-3}, & 0.51 Z$_\odot$, respectively. No Ca or Fe lines are detected from the nebula coincident with the EEx, but strong Mg, Ne, and O lines are (Tran et al. 2000), possibly as a result of metal depletion onto dust grains (*e.g.* Donahue & Voit 1993). Thus, a metal depleted, grain-rich, 12 kpc thick nebular slab was placed 15 kpc from an attenuated $\Gamma = 1.7$ power law source with power 1×10^{47} erg s^{-1}. Likewise, a 17 kpc $\times$ 16 kpc ICM slab was placed 19 kpc from the same source. The QSO radiation was attenuated using a 15 kpc column of density 0.06 cm^{-3}, abundance 0.51 Z$_\odot$, and temperature 3 keV. The output models were summed, folded through the *Chandra* responses using XSPEC, and fitted to the observed EEx spectrum (shown in Figure 5).

In the energy range 0.1-10.0 keV, the nebula emission lines which exceed the thermal line emission originate from Si, Cl, O, F, K, Ne, Co, Na, & Fe and occur as blends around redshifted 0.4, 0.6, 0.9, & 1.6 keV. The energies and strengths of these blends are in good agreement with the EEx spectrum. Further, the Fe Kα emission from the nebula is 100 times fainter than that from the ICM, and the observed asymmetry of the EEx Fe Kα emission results from the 6.4 keV Fe Kα photoionized line of the ICM. We conclude that the QSO is responsible for the nature of the EEx, but higher resolution radio observations are necessary to discern between beamed AGN radiation and QSO radiation escaping the obscured nucleus.

An alternative explanation for the EEx is that parcels of low entropy gas have been uplifted from deeper within the core along the new AGN beaming axis. Scattered UV emission 32 kpc from the core places a minimum lifetime of 73 kyr for the new beaming direction (H93), and, assuming saturated heat flux across the EEx

surface, the evaporation time is exceedingly short, < 1 Myr. These short timescales suggest the EEx was transported to the present location at > 20 times the ambient sound speed, or $v \sim 0.06$–$0.1c$, well below typical jet bulk flow velocities. The radio spur has a 1.4 GHz luminosity of $\approx 3 \times 10^{39}$ erg s^{-1}, suggesting an associated 1 Myr old jet would have $\sim 10^{57}$ erg of kinetic energy, which is sufficient to lift $\sim 10^{10}$ M$_\odot$ to a distance of 19 kpc. Uplift is feasible, particularly if the uplifted gas is magnetically-shielded, which will stave-off conduction.

8 NUCLEUS X-RAY EMISSION

Coordinates for the nuclear source were determined using the CIAO tool `wavdetect` and confirmed with a hardness ratio map calculated as $HR = f(2.0$–$9.0 \text{ keV})/f(0.5$–$2.0 \text{ keV})$, where f is the flux in the denoted energy band. The *HR* map and spectral extraction regions are shown in Figure 6. A source extraction region was defined using the 90% enclosed energy fraction (EEF) of the normalized *Chandra* PSF specific to the nuclear source median photon energy and off-axis position. The elliptical source region had an effective radius of 1.16″. A segmented elliptical annulus with the same central coordinates, ellipticity, and position angle as the source region, but having 5 times the area, was used for the background region. The background annulus was broken into segments to avoid the regions of excess X-ray emission.

Source and background spectra were created using the CIAO tool `psextract`. The source spectrum was grouped to have 20 counts per energy channel. Presented in Figure 6 are the 1999 and 2009 background-subtracted *Chandra* spectra and the best-fit models. The spectra have been corrected for soft Galactic emission and ICM emission. The significant flux difference below 1.3 keV is a result of the greater effective area of the ACIS-S3 CCD in 1999 versus ACIS-I3 in 2009. Approximately 72% of the 2009 spectrum (hereafter, SP09) is from the source, with a count rate of 1.63 (± 0.06) $\times 10^{-2}$ ct s^{-1} in the 0.5-9.0 keV band. For the 1999 spectrum (hereafter, SP99), 67% is source flux, with a count rate of 2.71 (± 0.26) $\times 10^{-2}$ ct s^{-1} in the 0.5-9.0 keV band.

Previous studies have shown the nuclear spectrum is best modeled as Compton reflection from cold matter with a ~ 1 keV equivalent width (EW) Fe Kα fluorescence line at rest-frame 6.4 keV (Tran et al. 2000; Iwasawa et al. 2001). Illumination of the AGN-facing side of a metal-rich circumnuclear torus is the favored explanation for the origin of Fe Kα fluorescence (Krolik et al. 1994). We confirm the conclusion of Iwasawa et al. (2001) that the contribution from thermal ICM Fe Kα emission to the line feature around 4.4 keV is negligible. The SP09 also reveals prominent features around 0.8 keV and 1.3 keV superposed on the reflection continuum. The relative strength and location of these features suggest they are emission line blends.

The SP99 and SP09 were fitted seperately in XSPEC over the energy range 0.5-7.0 keV with an absorbed PEXRAV model (Magdziarz & Zdziarski 1995) plus three Gaussians. The disk-reflection geometry employed in the PEXRAV model is not ideal for fitting reflection from a Compton-thick torus (Murphy & Yaqoob 2009), but no other suitable XSPEC model is currently available. Hence, only the PEXRAV reflection component was fitted and no high energy cut-off for the power law was used. Fitting separate SP99 and SP09 models allowed for source variation in the decade between observations, however Γ was poorly constrained for SP99 and thus fixed at the SP09 value. Using constraints from Tran et al. (2000), the model parameters for reflec-

tor abundance and source inclination were fixed at 1.0 $Z_\odot$ and $i = 50°$, respectively. Setting abundance as a free parameter did not statistically improve the fits. The best-fit model parameters are presented in Table 4. The unabsorbed 2-10 keV *reflected* flux is $4.24^{+0.57}_{-0.55} \times 10^{-13}$ erg s^{-1} cm^{-2} corresponding to a rest-frame $L_{2-10} = 1.57^{+0.19}_{-0.19} \times 10^{44}$ erg s^{-1}. Adjusted for cosmology, this agrees with the measurement from Iwasawa et al. (2001). Since we have used a pure reflection model, the intrinsic QSO luminosity can only be estimated as $(\kappa/\eta)L_{2-10}$ where $\kappa = 40$ is a bolometric correction factor (Vasudevan & Fabian 2007) and $\eta = 0.06$ is the reflector albedo (Murphy & Yaqoob 2009). This gives $L_{\rm bol}^{\rm QSO} = 1.05(\pm0.13) \times 10^{47}$ erg s^{-1}.

The EW$_{\rm K\alpha}$, is a valuable diagnostic for probing the environment of an AGN (see Fabian et al. 2000a, for a review). Our best-fit EW$_{\rm K\alpha}$ values agree with previous observations and models which show that EW$_{\rm K\alpha} \gtrsim 0.5$ keV is correlated with $\Gamma \gtrsim 1.7$ and reflecting column densities $N_{\rm H,ref} \sim 10^{24}$ cm^{-2} (Matt et al. 1996; Nandra et al. 1997; Zdziarski et al. 1999; Guainazzi et al. 2005). Our best-fit values for the IRAS09 EW$_{\rm K\alpha}$ also agree with previous measurements, which varied between 0.2–2 keV with ≈ 0.5 keV preferred (Franceschini et al. 2000; Iwasawa et al. 2001; Piconcelli et al. 2007). The large uncertainties and inhomogeneous spectral analyses of literature values prevents us from determining if EW$_{\rm K\alpha}$ has varied since 1998. However, fitting the R_{500} spectra from *Chandra*, *XMM-Newton*, and *BeppoSAX* with our SP09 and ICM models yielded satisfactory fits with EW$_{\rm K\alpha} < 0.9$ keV for all datasets.

Fitting the SP09 with a solar abundance thermal component in place of the two low-energy Gaussians yielded a statistically worse fit. The model systematically underestimated the 1-1.5 keV flux and overestimated the 2-4 keV flux. Leaving the thermal component abundance as a free parameter resulted in 0.1 $Z_\odot$, *i.e.* the thermal component tended toward a featureless skewed-Gaussian. Strong Mg, Ne, S, and Si Kα fluorescence lines at $E < 3.0$ keV can be present in reflection spectra (George & Fabian 1991), as can Fe L-shell lines from photoionized gas (Band et al. 1990). We conclude that the soft X-ray emission modeled using the Gaussians is likely a combination of emission line blends and low-level thermal continuum, whether the thermal component is nuclear or ambient in origin is unclear.

Previous studies suggested the *BeppoSAX* PDS detection resulted primarily from transmission of hard X-rays through an obscuring screen with $N_{\rm H,obs} > 10^{24}$ cm^{-2}. Extrapolating our SP09 model out to 10-80 keV reveals statistically acceptable agreement with the PDS data (see Figure 4). The 10-200 keV flux for the SP09 model is $f_{10-200} = 8.15^{+0.21}_{-0.19} \times 10^{-12}$ erg s^{-1} cm^{-2}, which is not significantly different from f_{10-200} measured with *BeppoSAX*. Adding a power-law component with a $N_{\rm H,obs} = 3 \times 10^{24}$ cm^{-2} absorber at the IRAS09 redshift to the SP09 model lowers χ^2 but with no statistical improvement to the fit. If transmitted hard X-ray emission fell within the passband used for analysis of the reflection spectrum, then lower values of Γ would result, and the extrapolated hard X-ray flux would increase. However, for $\Gamma \geqslant 1.7$, column densities $> 3 \times 10^{24}$ cm^{-2} are sufficient to suppress significant transmitted emission below our 7 keV analysis cut-off, indicating the SP09 model should not have an artifically low Γ. That we find no need for an additional hard X-ray component does not contradict the conclusion that IRAS09 harbors a Compton-thick AGN. The measured EW$_{\rm K\alpha}$ suggests reflecting column densities of $N_{\rm H,ref} \sim 1$–5×10^{24} cm^{-2} (Leahy & Creighton 1993; Guainazzi et al. 2005), assuming the nuclear material is mostly ho-

mogeneous, *i.e.* $N_{\rm H,ref} \approx N_{\rm H,obs}$, our results are consistent with the prescence of a heavily obscured AGN.

9 SUMMARY

We have presented analysis of the ULIRG IRAS 09104+4109 and the host galaxy cluster RX J0913.7+4056 using a new 75 ks *Chandra* X-ray observation. The results presented in this paper are as follows:

• The RX J0913.7+4056 ICM global and radial properties reveal no signs of shocks, cold fronts, deviations from hydrostatic equilibrium, or the like, to suggest disruption by a major merger or cluster-scale AGN outburst. RX J0913.7+4056 is an unremarkable, massive, cool core object with a 12 keV cm^2 core entropy, $M \propto T^{3/2}$, and mean gas fraction of 0.11.

• Using the RX J0913.7+4056 gas density profile, we have determined that the measured BCG gas mass is at odds with the amount of gas which can be efficiently removed from cluster members via the process of ram pressure stripping also find that tidal stripping is an unlikely explanation for the nature of spheroids found in the cluster core, further suggesting that subcluster mergers are an unlikely source for the gas reservoir in IRAS09. The highly linear radio source morphology further indicates that merger activity has ceased for at least the last 22 Myr.

• We have discovered cavities in the X-ray halo of IRAS09 which indicate an AGN outburst with mechanical energy of at least 3.41×10^{44} erg s^{-1}, a hundredth of the QSO radiative energy. Comparison of cavity sound speed age and radio source age indicate the outflow is supersonic with $M = 2.3$, suggesting the total kinetic energy may be $\sim 10^{46}$ erg s^{-1}.

• We have determined that cold-mode accretion is a preferable explanation for the nature of IRAS09. We also show that the QSO has a high effective Eddington luminosity of ≈ 0.9, indicating radiation pressure should be expelling dusty clouds from IRAS09.

• We have resolved substructure in the X-ray halo coincident with the [O III] nebula NE of the nucleus. The X-ray emission properties of this region are well-fit by a model where the nebula and ICM are irradiated by the QSO.

• The nuclear X-ray source is well-fit by a reflection model resulting from a $\Gamma = 1.7$ power law source. The EW$_{\rm K\alpha}$ indicates a reflecting column density, and presumably obscuring column density, of $> 10^{24}$ cm^{-2}. We also show that the *BeppoSAX* detected hard X-ray emission results from reflected nuclear emission.

IRAS09 simultanesouly shows the characteristics of a system in quasar- and radio-mode. The photoionized region NE of the nucleus, high $\lambda_{\rm Edd}$, low gas-to-dust ratio, and strong nuclear optical outflow all suggest the central 30 kpc of RX J0913.7+4056 is dominated by radiative feedback from the QSO in IRAS09. At the same time, the X-ray cavities and radio outflow show an AGN actively suppressing cooling of the ICM. IRAS09 may be a local example of how massive galaxies at higher redshifts evolve from quasar-mode into radio-mode.

REFERENCES

Allen S. W., 2000, MNRAS, 315, 269 4

Anders E., Grevesse N., 1989, Geochim. Cosmochim. Acta, 53, 197 2

Armus L., Soifer B. T., Neugebauer G., 1999, Ap&SS, 266, 113 5, 6, 7

Arnaud K. A., 1996, in Astronomical Society of the Pacific Conference Series, Vol. 101, Astronomical Data Analysis Software and Systems V, Jacoby G. H., Barnes J., eds., pp. 17–+ 2

Arnaud M., Aghanim N., Neumann D. M., 2002, A&A, 389, 1 4

Band D. L., Klein R. I., Castor J. I., Nash J. K., 1990, ApJ, 362, 90 8

Bassani L., Molina M., Malizia A., Stephen J. B., Bird A. J., Bazzano A., Bélanger G., Dean A. J., De Rosa A., Laurent P., Lebrun F., Ubertini P., Walter R., 2006, ApJ, 636, L65 3

Bîrzan L., McNamara B. R., Nulsen P. E. J., Carilli C. L., Wise M. W., 2008, ApJ, 686, 859 5

Bîrzan L., Rafferty D. A., McNamara B. R., Wise M. W., Nulsen P. E. J., 2004, ApJ, 607, 800 5

Blanton E. L., Randall S. W., Douglass E. M., Sarazin C. L., Clarke T. E., McNamara B. R., 2009, ApJ, 697, L95 6

Bower R. G., McCarthy I. G., Benson A. J., 2008, MNRAS, 390, 1399 1

Carilli C. L., Perley R. A., Dreher J. W., Leahy J. P., 1991, ApJ, 383, 554 3

Cash W., 1979, ApJ, 228, 939 6

Cavagnolo K. W., Donahue M., Voit G. M., Sun M., 2008a, ApJ, 683, L107 4

—, 2008b, ApJ, 682, 821 4

—, 2009a, ApJS, 182, 12 4

Cavagnolo K. W., McNamara B. R., Carilli C. L., Jones C., Forman W. R., Nulsen P. E. J., Bîrzan L., Murray S., 2009b, In preparation for ApJ 5

Cavaliere A., Fusco-Femiano R., 1978, A&A, 70, 677 4

Cohen A. S., Lane W. M., Cotton W. D., Kassim N. E., Lazio T. J. W., Perley R. A., Condon J. J., Erickson W. C., 2007, AJ, 134, 1245 3

Crawford C. S., Vanderriest C., 1996, MNRAS, 283, 1003 1, 2, 5, 7

Croton D. J., Springel V., White S. D. M., De Lucia G., Frenk C. S., Gao L., Jenkins A., Kauffmann G., Navarro J. F., Yoshida N., 2006, MNRAS, 365, 11 1

Deane J. R., Trentham N., 2001, MNRAS, 326, 1467 1

Donahue M., Horner D. J., Cavagnolo K. W., Voit G. M., 2006, ApJ, 643, 730 6

Donahue M., Voit G. M., 1993, ApJ, 414, L17 7

Dunn R. J. H., Fabian A. C., Taylor G. B., 2005, MNRAS, 364, 1343 5

Edge A. C., 2001, MNRAS, 328, 762 1

Evans A. S., Sanders D. B., Cutri R. M., Radford S. J. E., Surace J. A., Solomon P. M., Downes D., Kramer C., 1998, ApJ, 506, 205 1

Faber S. M., Jackson R. E., 1976, ApJ, 204, 668 6

Fabian A. C., Crawford C. S., 1995, MNRAS, 274, L63 5

Fabian A. C., Iwasawa K., Reynolds C. S., Young A. J., 2000a, PASP, 112, 1145 8

Fabian A. C., Sanders J. S., Ettori S., Taylor G. B., Allen S. W., Crawford C. S., Iwasawa K., Johnstone R. M., Ogle P. M., 2000b, MNRAS, 318, L65 1

Fabian A. C., Shioya Y., Iwasawa K., Nandra K., Crawford C., Johnstone R., Kunieda H., McMahon R., Makishima K., Murayama T., Ohashi T., Tanaka Y., Taniguchi Y., Terashima Y., 1994, ApJ, 436, L51 1

Fabian A. C., Vasudevan R. V., Mushotzky R. F., Winter L. M., Reynolds C. S., 2009, MNRAS, 394, L89 6

Ferland G. J., Korista K. T., Verner D. A., Ferguson J. W., Kingdon J. B., Verner E. M., 1998, PASP, 110, 761 7

Ferrari C., Govoni F., Schindler S., Bykov A. M., Rephaeli Y., 2008, Space Science Reviews, 134, 93 4

Franceschini A., Bassani L., Cappi M., Granato G. L., Malaguti G., Palazzi E., Persic M., 2000, A&A, 353, 910 1, 2, 8

George I. M., Fabian A. C., 1991, MNRAS, 249, 352 8

Graham A. W., 2007, MNRAS, 379, 711 6

Guainazzi M., Matt G., Perola G. C., 2005, A&A, 444, 119 8

Heavens A. F., Meisenheimer K., 1987, MNRAS, 225, 335 3

Hines D. C., Schmidt G. D., Wills B. J., Smith P. S., Sowinski L. G., 1999, ApJ, 512, 145 7, 15

Hines D. C., Wills B. J., 1993, ApJ, 415, 82 1, 3

Iwasawa K., Fabian A. C., Ettori S., 2001, MNRAS, 321, L15 1, 7, 8

Jaffe W. J., Perola G. C., 1973, A&A, 26, 423 3

Kalberla P. M. W., Burton W. B., Hartmann D., Arnal E. M., Bajaja E., Morras R., Pöppel W. G. L., 2005, A&A, 440, 775 2

Kardashev N. S., 1962, Soviet Astronomy, 6, 317 3

Kirkpatrick C. C., McNamara B. R., Rafferty D. A., Nulsen P. E. J., Bîrzan L., Kazemzadeh F., Wise M. W., Gitti M., Cavagnolo K. W., 2009, ApJ, 697, 867 5

Kleinmann S. G., Hamilton D., Keel W. C., Wynn-Williams C. G., Eales S. A., Becklin E. E., Kuntz K. D., 1988, ApJ, 328, 161 1

Kriss G. A., Cioffi D. F., Canizares C. R., 1983, ApJ, 272, 439 4

Krolik J. H., Madau P., Zycki P. T., 1994, ApJ, 420, L57 7

Leahy D. A., Creighton J., 1993, MNRAS, 263, 314 8

Magdziarz P., Zdziarski A. A., 1995, MNRAS, 273, 837 7

Marconi A., Hunt L. K., 2003, ApJ, 589, L21 6

Matt G., Brandt W. N., Fabian A. C., 1996, MNRAS, 280, 823 8

Maughan B. J., 2007, ApJ, 668, 772 4

McGill K. L., Woo J., Treu T., Malkan M. A., 2008, ApJ, 673, 703 6

McNamara B. R., Nulsen P. E. J., 2007, ARA&A, 45, 117 1, 5

McNamara B. R., Nulsen P. E. J., Wise M. W., Rafferty D. A., Carilli C., Sarazin C. L., Blanton E. L., 2005, Nature, 433, 45 1

McNamara B. R., Rohanizadegan M., Nulsen P. E. J., 2010, In preparation for ApJL 6

Mewe R., Gronenschild E. H. B. M., van den Oord G. H. J., 1985, A&AS, 62, 197 2

Mewe R., Lemen J. R., van den Oord G. H. J., 1986, A&AS, 65, 511 2

Miley G., 1980, ARA&A, 18, 165 3

Murphy K. D., Yaqoob T., 2009, MNRAS, 397, 1549 7, 8

Nandra K., George I. M., Mushotzky R. F., Turner T. J., Yaqoob T., 1997, ApJ, 477, 602 8

Narayanan D., Cox T. J., Robertson B., Davé R., Di Matteo T., Hernquist L., Hopkins P., Kulesa C., Walker C. K., 2006, ApJ, 642, L107 1

Nousek J. A., Shue D. R., 1989, ApJ, 342, 1207 6

Pacholczyk A. G., 1970, Radio astrophysics. Nonthermal processes in galactic and extragalactic sources, Pacholczyk A. G., ed. 3

Peeters E., Spoon H. W. W., Tielens A. G. G. M., 2004, ApJ, 613, 986 1

Piconcelli E., Fiore F., Nicastro F., Mathur S., Brusa M., Comastri A., Puccetti S., 2007, A&A, 473, 85 2, 8

Pizzolato F., Soker N., 2005, ApJ, 632, 821 6

—, 2010, ArXiv e-prints 6

Pratt G. W., Croston J. H., Arnaud M., Böhringer H., 2009, A&A, 498, 361 4

Reiprich T. H., Böhringer H., 2002, ApJ, 567, 716 4

Rengelink R. B., Tang Y., de Bruyn A. G., Miley G. K., Bremer M. N., Roettgering H. J. A., Bremer M. A. R., 1997, A&AS, 124, 259 3

Riley J. M. W., Waldram E. M., Riley J. M., 1999, MNRAS, 306, 31 3

Russell H. R., Fabian A. C., Sanders J. S., Johnstone R. M., Blundell K. M., Brandt W. N., Crawford C. S., 2010, MNRAS, 402, 1561 7

Sargsyan L., Mickaelian A., Weedman D., Houck J., 2008, ApJ, 683, 114 1

Schawinski K., Lintott C. J., Thomas D., Kaviraj S., Viti S., Silk J., Maraston C., Sarzi M., Yi S. K., Joo S., Daddi E., Bayet E., Bell T., Zuntz J., 2009, ApJ, 690, 1672 1

Scheuer P. A. G., Williams P. J. S., 1968, ARA&A, 6, 321 4

Simionescu A., Roediger E., Nulsen P. E. J., Brüggen M., Forman W. R., Böhringer H., Werner N., Finoguenov A., 2009, A&A, 495, 721 5

Simionescu A., Werner N., Forman W. R., Miller E. D., Takei Y., Böhringer H., Churazov E., Nulsen P. E. J., 2010, ArXiv e-prints 5

Slee O. B., Roy A. L., Murgia M., Andernach H., Ehle M., 2001, AJ, 122, 1172 3

Soifer B. T., Neugebauer G., Armus L., Shupe D. L., 1996, AJ, 111, 649 5

Soker N., 2006, New Astronomy, 12, 38 6

Springel V., White S. D. M., Jenkins A., Frenk C. S., Yoshida N., Gao L., Navarro J., Thacker R., Croton D., Helly J., Peacock J. A., Cole S., Thomas P., Couchman H., Evrard A., Colberg J., Pearce F., 2005, Nature, 435, 629 1

Sun M., Jones C., Forman W., Vikhlinin A., Donahue M., Voit M., 2007, ApJ, 657, 197 6

Taniguchi Y., Sato Y., Kawara K., Murayama T., Mouri H., 1997, A&A, 318, L1 1

Tran H. D., Cohen M. H., Villar-Martin M., 2000, AJ, 120, 562 5, 7

Tremaine S., Gebhardt K., Bender R., Bower G., Dressler A., Faber S. M., Filippenko A. V., Green R., Grillmair C., Ho L. C., Kormendy J., Lauer T. R., Magorrian J., Pinkney J., Richstone D., 2002, ApJ, 574, 740 6

Tueller J., Baumgartner W. H., Markwardt C. B., Skinner G. K., Mushotzky R. F., Ajello M., Barthelmy S., Beardmore A., Brandt W. N., Burrows D., Chincarini G., Campana S., Cummings J., Cusumano G., Evans P., Fenimore E., Gehrels N.,

Godet O., Grupe D., Holland S., Kennea J., Krimm H. A., Koss M., Moretti A., Mukai K., Osborne J. P., Okajima T., Pagani C., Page K., Palmer D., Parsons A., Schneider D. P., Sakamoto T., Sambruna R., Sato G., Stamatikos M., Stroh M., Ukwata T., Winter L., 2010, ApJS, 186, 378 3

Vasudevan R. V., Fabian A. C., 2007, MNRAS, 381, 1235 8

Vikhlinin A., Kravtsov A., Forman W., Jones C., Markevitch M., Murray S. S., Van Speybroeck L., 2006, ApJ, 640, 691 4

Vikhlinin A., Markevitch M., Murray S. S., Jones C., Forman W., Van Speybroeck L., 2005, ApJ, 628, 655 4

Voit G. M., Cavagnolo K. W., Donahue M., Rafferty D. A., McNamara B. R., Nulsen P. E. J., 2008, ApJ, 681, L5 4

Waters C. Z., Zepf S. E., 2005, ApJ, 624, 656 3

Xue Y.-J., Wu X.-P., 2000, MNRAS, 318, 715 5

Zdziarski A. A., Lubinski P., Smith D. A., 1999, MNRAS, 303, L11 8

Table 1. SUMMARY OF GLOBAL ICM SPECTRAL FITS.

Region	R_{in}	R_{out}	kT_X	L_{bol}	Z	$\chi^2_{red.}$	D.O.F.	% Source	η	Ct. Rate
-	kpc	kpc	keV	10^{44} erg s^{-1}	$Z_\odot$	-	-	-	10^{-4} cm^{-5}	ct s^{-1}
(1)	(2)	(3)	(4)	(5)	(6)	(7)	(8)	(9)	(10)	(11)
$R_{200-Core}$	174	1835	$10.22^{+5.38}_{-2.65}$	$7.95^{+1.50}_{-1.80}$	0.38†	1.13	429	15	$8.50^{+4\%}_{-4\%}$	0.066
$R_{500-Core}$	174	1160	$7.54^{+1.76}_{-1.15}$	$6.90^{+0.61}_{-0.59}$	$0.38^{+0.31}_{-0.17}$	1.01	277	27	$8.24^{+6\%}_{-6\%}$	0.063
$R_{1000-Core}$	174	820	$6.80^{+1.14}_{-0.88}$	$6.17^{+0.41}_{-0.57}$	0.38†	1.05	219	38	$7.90^{+3\%}_{-3\%}$	0.058
$R_{2500-Core}$	174	519	$7.18^{+1.25}_{-0.93}$	$5.18^{+0.41}_{-0.38}$	0.38†	1.06	150	56	$6.48^{+3\%}_{-3\%}$	0.048
$R_{5000-Core}$	174	367	$6.40^{+1.01}_{-0.80}$	$3.80^{+0.44}_{-0.26}$	0.38†	1.01	104	67	$4.99^{+4\%}_{-3\%}$	0.036
R_{200}	13	1835	$6.02^{+0.45}_{-0.40}$	$25.6^{+2.7}_{-2.4}$	$0.41^{+0.10}_{-0.11}$	1.00	498	34	$34.4^{+2\%}_{-2\%}$	0.240
R_{500}	13	1160	$5.61^{+0.32}_{-0.30}$	$24.8^{+2.9}_{-2.5}$	$0.43^{+0.09}_{-0.08}$	0.78	357	54	$34.1^{+2\%}_{-2\%}$	0.237
R_{1000}	13	820	$5.49^{+0.28}_{-0.26}$	$24.2^{+2.6}_{-2.4}$	$0.40^{+0.08}_{-0.08}$	0.80	306	68	$33.8^{+2\%}_{-2\%}$	0.232
R_{2500}	13	519	$5.50^{+0.27}_{-0.25}$	$23.1^{+2.5}_{-2.0}$	$0.39^{+0.07}_{-0.07}$	0.82	265	83	$32.4^{+2\%}_{-2\%}$	0.222
R_{5000}	13	367	$5.34^{+0.25}_{-0.23}$	$21.8^{+2.1}_{-1.9}$	$0.39^{+0.07}_{-0.07}$	0.80	241	90	$30.9^{+2\%}_{-2\%}$	0.210
R_{cool}	13	128	$4.94^{+0.24}_{-0.22}$	$16.1^{+2.5}_{-2.0}$	$0.42^{+0.08}_{-0.08}$	0.89	208	98	$22.9^{+3\%}_{-3\%}$	0.155

The nuclear region emits strong Fe Kα emission which affects the spectral fitting, and for apertures including the core, the nucleus was excluded using a region twice the size of the 90% *Chandra* PSF enclosed energy fraction (see Section 8 for details). A dagger (†) indicates core-excised regions fit with Z fixed at the iteratively determined value for $R_{500-Core}$. Bolometric luminosities were determined using a diagonalized response function over the energy range 0.01-100.0 keV with 5000 linearly spaced energy channels. Col. (1) Spectral extraction region; Col. (2) Inner radius; Col. (3) Outer radius; Col. (4) Gas temperature; Col. (5) Unabsorbed bolometric luminosity; Col. (6) Gas abundance; Col. (7) Reduced χ^2; Col. (8) Degrees of freedom; Col. (9) Percentage of emission attributable to source; Col. (10) Model normalization; Col. (11) Background-subtracted count rate.

Table 2. SUMMARY OF X-RAY EXCESSES SPECTRAL FITS.

Region	kT_X	η	E_G	σ_G	η_G	Cash	DOF
-	keV	10^{-5} cm^{-5}	keV	keV	10^{-6} cm^{-2} s^{-1}	-	-
(1)	(2)	(3)	(4)	(5)	(6)	(7)	(8)
EEx	$3.03^{+1.19}_{-0.74}$	$5.80^{+1.07}_{-0.97}$	-	-	-	524	512
EEx	$3.68^{+3.34}_{-1.58}$	$2.73^{+0.98}_{-0.94}$	[0.89, 1.42, 4.23]	[0.04, 0.16, 3.6E − 4]	[1.2, 2.0, 0.16]	384	512
EEx Bgd	$3.92^{+0.35}_{-0.31}$	$39.9^{+0.18}_{-0.17}$	-	-	-	471	512
WEx	$2.55^{+2.61}_{-0.98}$	$0.66^{+0.11}_{-0.07}$	-	-	-	387	512

Metal abundance was fixed at 0.51 $Z_\odot$ for all fits. Col. (1) Extraction region; Col. (2) Thermal gas temperature; Col. (3) Model normalization; Col. (4) Gaussian central energies; Col. (5) Gaussian dispersions; Col. (6) Gaussian normalizations; Col. (7) Modified Cash statistic; Col. (8) Degrees of freedom.

Table 3. SUMMARY OF CAVITY PROPERTIES.

Region	r	l	t_{sonic}	$t_{buoyant}$	t_{refill}	pV	H_{cav}	P_{cav}
–	kpc	kpc	10^7 yr	10^7 yr	10^7 yr	10^{58} ergs	10^{59} ergs	10^{44} ergs s^{-1}
(1)	(2)	(3)	(4)	(5)	(6)	(7)	(8)	(9)
NW	6.40 ± 0.64	58.3 ± 5.8	5.05 ± 0.76	9.92 ± 1.22	18.6 ± 2.3	6.50 ± 0.70	2.60 ± 0.28	1.63 ± 0.30
SE	6.81 ± 0.68	64.0 ± 6.4	5.54 ± 0.84	10.9 ± 1.3	20.3 ± 2.5	7.76 ± 0.85	3.10 ± 0.34	1.78 ± 0.33

Col. (1) Cavity location; Col. (2) Radius of excavated cylinder; Col. (3) Length of excavated cylinder; Col. (4) Sound speed age; Col. (5) Buoyant rise time age; Col. (6) Volume refilling age; Col. (7) pV work; Col. (8) Cavity enthalpy; Col. (9) Cavity power using sonic age.

Table 4. SUMMARY OF NUCLEAR SOURCE SPECTRAL FITS.

Component	Parameter	2009	1999
(1)	(2)	(3)	(4)
PEXRAV	Γ	$1.71^{+0.23}_{-0.65}$	fixed to 2009
-	η_P	$8.07^{+0.64}_{-0.62} \times 10^{-4}$	$8.46^{+2.08}_{-2.12} \times 10^{-4}$
GAUSSIAN 1	E_G	$0.73^{+0.05}_{-0.24}$	$0.61^{+0.10}_{-0.05}$
-	σ_G	85^{+197}_{-53}	97^{+150}_{-97}
-	η_G	$8.14^{+3.74}_{-5.82} \times 10^{-6}$	$1.65^{+1.52}_{-1.00} \times 10^{-5}$
GAUSSIAN 2	E_G	$1.16^{+0.19}_{-0.33}$	$0.90^{+0.17}_{-0.90}$
-	σ_G	383^{+610}_{-166}	506^{+314}_{-262}
-	η_G	$1.03^{+3.22}_{-0.48} \times 10^{-5}$	$1.48^{+2.68}_{-1.16} \times 10^{-5}$
GAUSSIAN 3	E_G	$4.45^{+0.04}_{-0.04}$	$4.46^{+0.04}_{-0.07}$
-	σ_G	45^{+60}_{-45}	31^{+94}_{-31}
-	η_G	$2.67^{+0.91}_{-0.86} \times 10^{-6}$	$6.45^{+4.17}_{-3.69} \times 10^{-6}$
-	$EW^{corr}_{K\alpha}$	531^{+211}_{-218}	1210^{+720}_{-710}
Statistics	χ^2	79.0	7.9
-	DOF	74	15

Fe Kα equivalent widths have been corrected for redshift. Units for parameters: Γ is dimensionless, η_P is in photons keV^{-1} cm^{-2} s^{-1}, E_G are in keV, σ_G are in eV, η_G are in photons cm^{-2} s^{-1}, EW_{corr} are in eV. Col. (1) XSPEC model name; Col. (2) Model parameters; Col. (3) Values for 2009 *Chandra* spectrum; Col. (4) Values for 1999 *Chandra* spectrum.
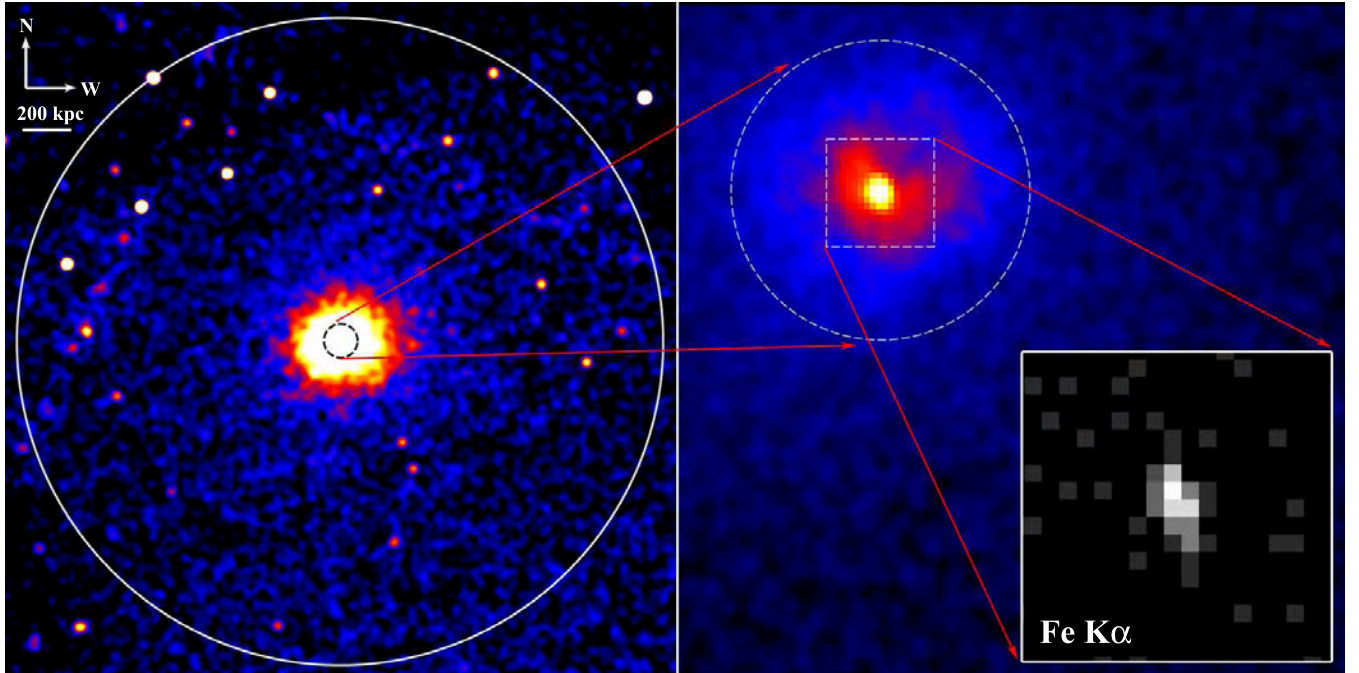

Figure 1. *Left*: *Chandra* 0.5-10.0 keV exposure-corrected mosaic image of the RX J0913.7+4056 ICM. Image is smoothed with 5″ Gaussian. White circle marks R_{500} and dashed circle at center of image has a diameter of 140 kpc. *Right*: 0.5-10.0 keV exposure-corrected mosaic image of the RX J0913.7+4056 core with an inset of the 4.35-4.5 keV emission from a box 25 kpc on a side. The core image is smoothed with a 1″ Gaussian while the inset is unsmoothed. The presence of cavity like structures to the northwest and southeast of the cD galaxy are evident. The inset image isolates Fe Kα flourescence line emission of material surrounding the AGN. Areas in black have 0 ct, and the darkest gray areas have 1 ct. The emission is consistent with the *Chandra* PSF, *i.e.* the source is not extended.
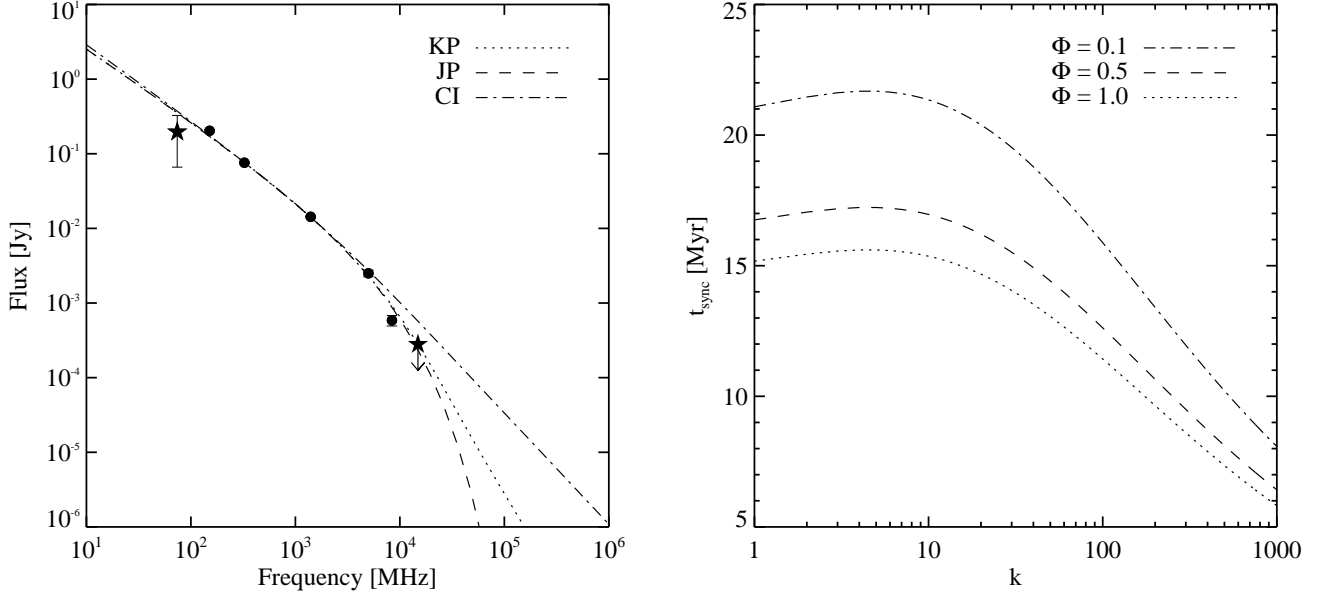
Figure 2. *Left*: Best-fit synchrotron models for the radio spectrum of IRAS 09104+4109. Stars denote points excluded in fitting. Plotted fluxes are for the full radio source, and the uncertainties are 1σ. The 1σ upper limit for the 14.9 GHz flux is shown. *Right*: Synchrotron age as a function of *k*, the ratio of lobe energy in non-radiating particles to that in relativistic electrons, for three values of Φ, the volume filling factor of the radiating particle population.
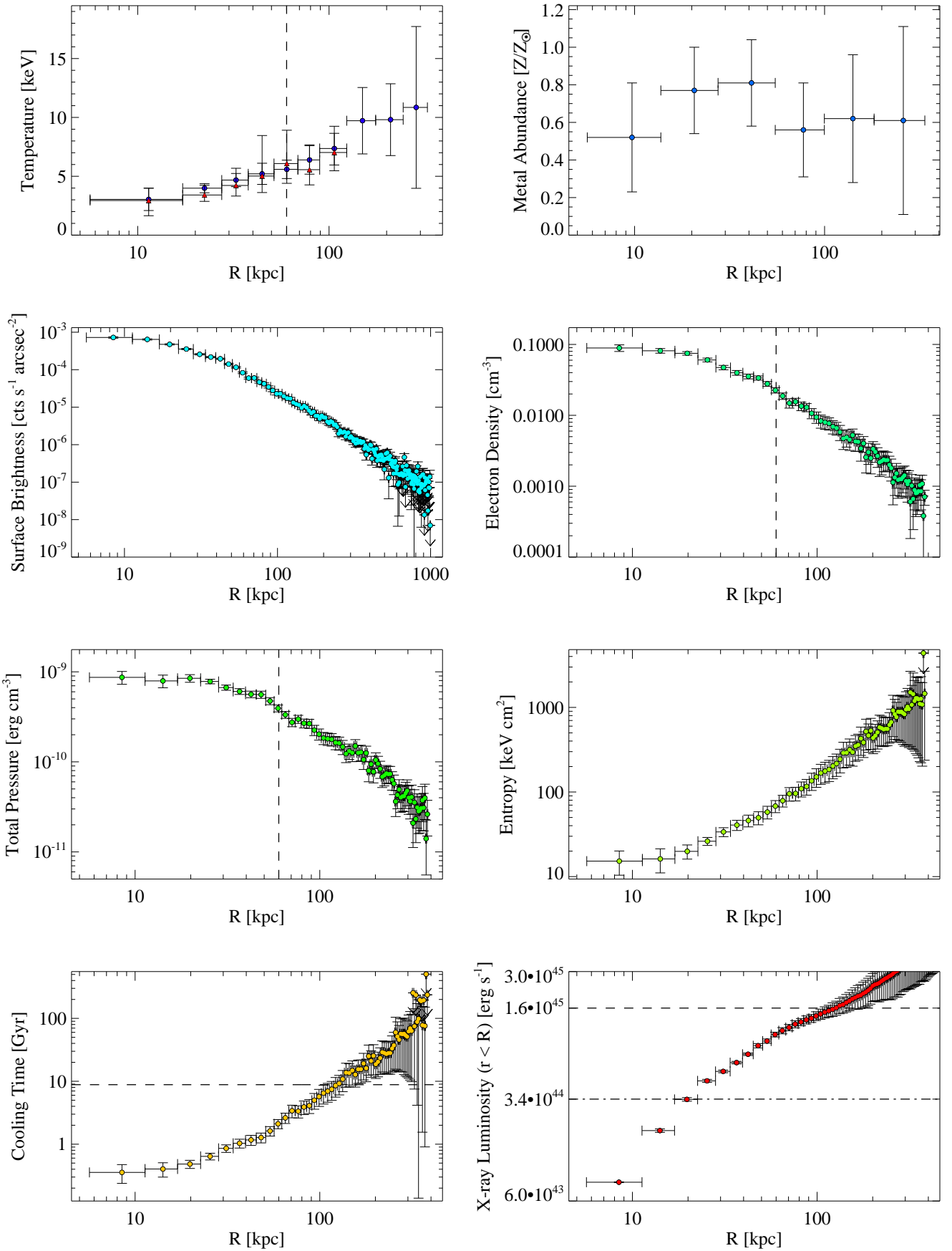
Figure 3. Gallery of radial ICM profiles. Vertical black dashed lines mark the approximate end-points of both cavities. Horizontal dashed line on cooling time profile marks age of the Universe at a redshift of $z = 0.4418$. For X-ray luminosity profile, dashed line marks L_{cool}, and dashed-dotted line marks P_{cav}.
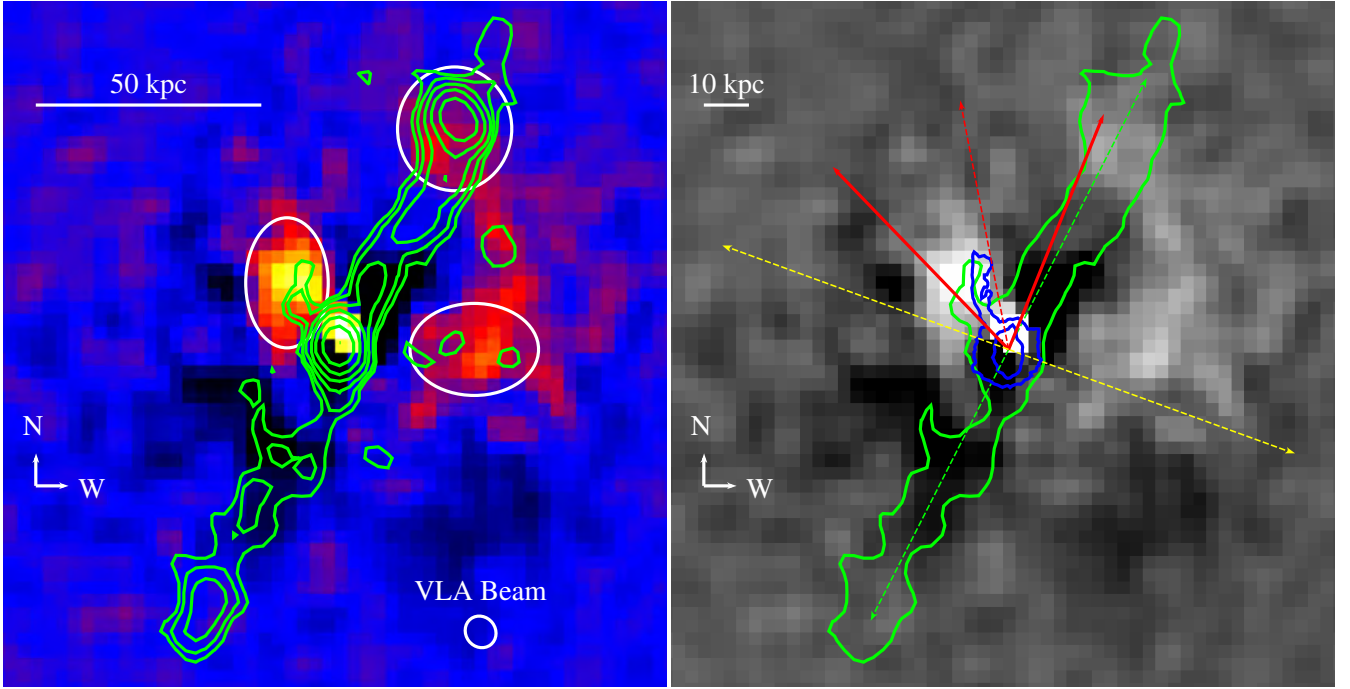
Figure 4. *Left*: Residual X-ray image after subtracting an elliptical surface brightness model from the parent image in the right panel of Figure 1. Green contours trace the 1.4 GHz radio emission in log-space steps beginning at $3\sigma_{RMS}$ and ending at 4.7 mJy beam^{-1}. Notice that the channels carved out in the X-ray gas by the AGN radio source are now obvious as cylindrical voids. The three white ellipses highlight regions of interest which are discussed in Section 7. *Right*: Same residual X-ray image as left panel, but in grayscale. The green contour traces 1.4 GHz radio emission at $3\sigma_{RMS}$, and the dashed green line shows the jet axis. Blue contours trace $\lambda_{\rm rest} \approx 3900 - 6650$ Å emission as seen with *HST*. The red dashed line shows the mean direction of the UV scattering bicone (see Hines et al. 1999, for discussion), while the solid red lines show the 1σ limits of the bicone opening angle.
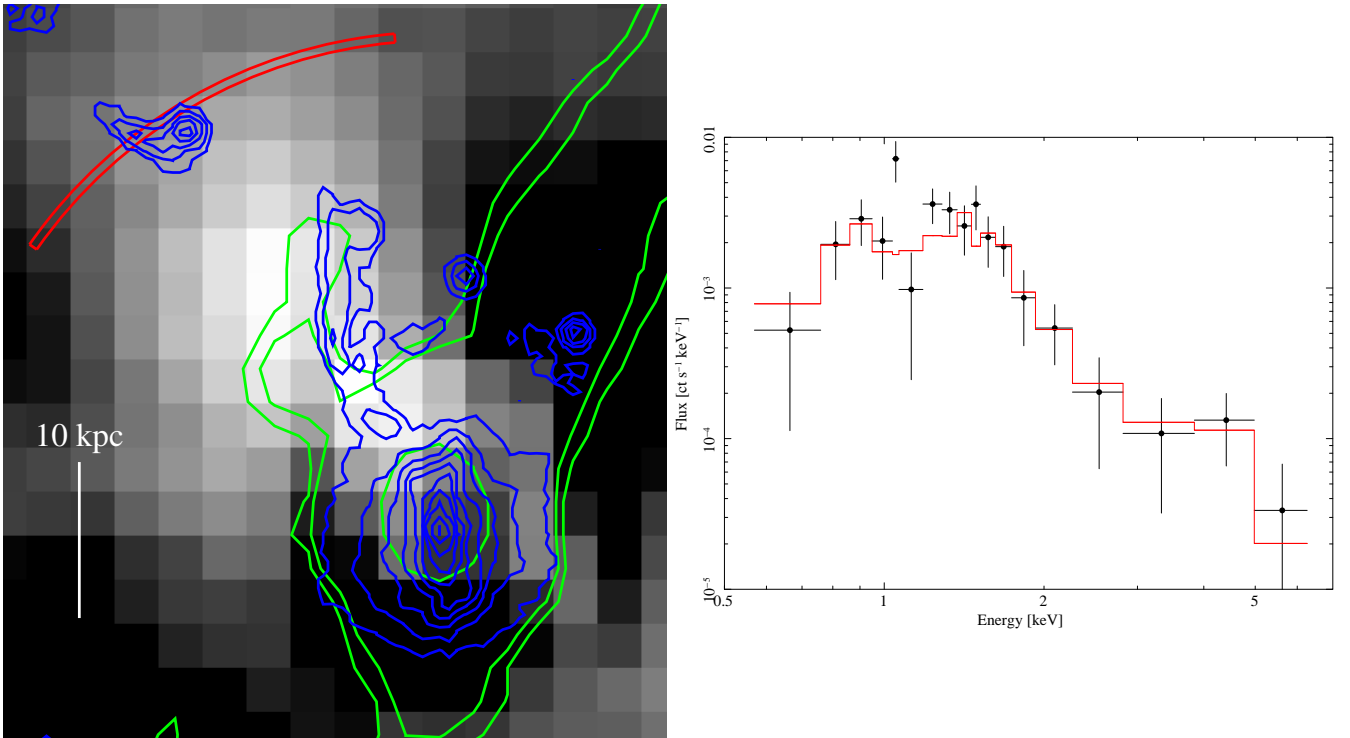

Figure 5. *Left:* Zoom-in of EEx overlaid with radio (green) and optical (blue) contours. Red wedge marks the extent of scattered UV emission. *Right:* Background-subtracted EEx spectrum binned to 3σ significance. The red line is the best-fit CLOUDY model for a QSO irradiated nebula and ICM.
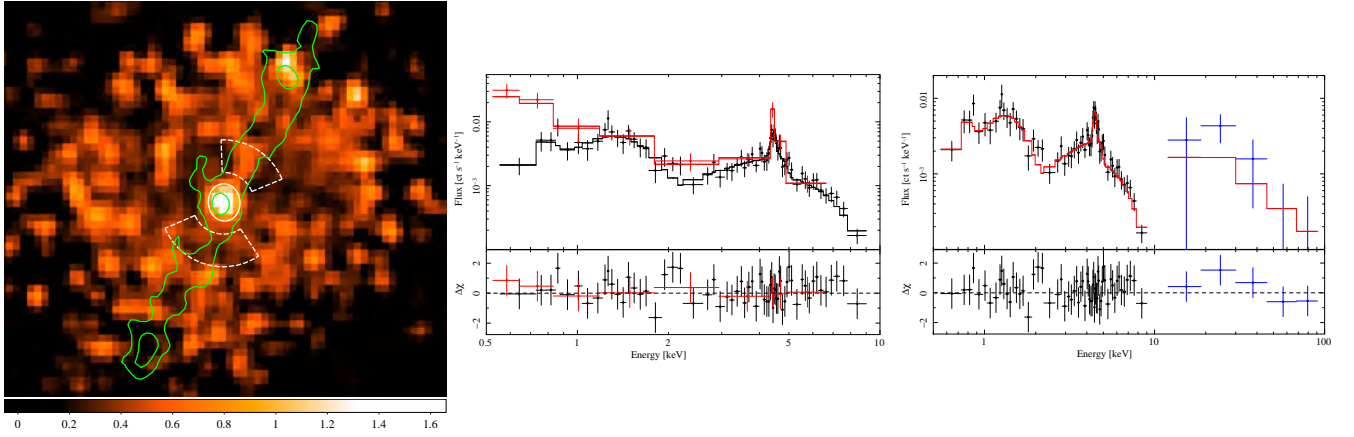
Figure 6. *Left: Chandra* hardness ratio (HR) map of the ICM surrounding IRAS 09104+4109. Green contours trace the highest and lowest significance 1.4 GHz emission regions. White ellipse is the 90% EEF source extraction region and dashed white wedges are regions used for background extraction. The areas with the largest *HR* are coincident with the central source and the termination point of the northern radio jet. *Middle:* Background-subtracted nuclear spectrum for the 1999 (red points) and 2009 (black points) *Chandra* observations. Data has been binned to 3σ significance. *Right:* Background-subtracted nuclear spectrum for the 2009 *Chandra* data (black points) and 1998 *BeppoSAX* PDS data (blue points). The red line is the extrapolated best-fit SP09 model.